Nanoscale

ARTICLE

Oxygen Self-doped g-C_3N_4 with Tunable Electronic Band Structure for Unprecedentedly Enhanced Photocatalytic Performance

Received 00th January 20xx,
Accepted 00th January 20xx

DOI: 10.1039/x0xx00000x

www.rsc.org/

Fangyan Wei,[a] Yang Liu,[a] Heng Zhao,[a] Xiaoning Ren,[a] Jing Liu,[a] Tawfique Hasan,[b] Lihua Chen,[a] Yu Li*[a] and Bao-Lian Su[acd]

As a fascinating conjugated polymer, graphitic carbon nitride (g-C_3N_4) has attracted much attention for solving the worldwide energy shortage and environmental pollution. In this work, for the first time we report oxygen self-doping of solvothermally synthesized g-C_3N_4 nanospheres with tunable electronic band structure *via* ambient air exposure for unprecedentedly enhanced photocatalytic perfromance. Various measurements, such as XPS, Mott–Schottky plots, and density functional theory (DFT) calculations reveal that such oxygen doping can tune the intrinsic electronic state and band structure of g-C_3N_4 *via* the formation of C-O-C bond. Our results show that the oxygen doping content can be controlled by the copolymerization of the precursors. As a consequence, the oxygen doped g-C_3N_4 shows excellent photocatalytic performance, with an RhB photodegradation rate of 0.249 min^{-1} and a hydrogen evolution rate of 3174 µmol h^{-1} g^{-1}, >35 times and ~4 times higher than that of conventional thermally made pure g-C_3N_4 (0.007 min^{-1} and 846 µmol h^{-1} g^{-1}, respectively) under visible light. Our work introduces a new route for the rational design and fabrication of doping modified g-C_3N_4 photocatalyst for efficient degradation of organic pollutants and H_2 production.

Introduction

Graphitic carbon nitride (g-C_3N_4), a metal-free polymeric organic semiconductor, has attracted significant attention due to its excellent performance in photocatalytic degradation of organic pollutants and H_2 production. g-C_3N_4 has a band gap of ~2.7 eV and a structure of 2D sheets, interconnected tri-3s-triazine *via* tertiary amines, which is capable of exhibiting strong oxidation and reduction in the visible light region, leading to its high photocatalytic activity for the degradation of organic pollutants and water splitting under visible light.[1, 2] However, limited optical absorption,[3, 4] fast photogenerated carriers recombination[5-7] and low electrical conductivity of bulk g-C_3N_4,[8, 9] etc., hinder its practical applications. Modulating the intrinsic band gap structure to broaden light response region and enhance the separation efficiency of photogenerated electrons and holes is a promising routine to significantly improve its photocatalytic performance.

In this context, non-metal (B, O, S, I) doping of g-C_3N_4 to substitute the C or N atoms has been widely adopted to effectively modulate the intrinsic band gap structure to extend the light absorption and adjust the redox potentials of g-C_3N_4 to promote the photocatalytic performance under visible light.[10-13] For example, Wang et al.[13] reported a calcination method at 550 °C to prepare iodine doped g-C_3N_4, which improved the optical absorption between 420 to 650 nm as the doping contents increased. Recently, numerous efforts have been made to develop oxygen doped g-C_3N_4 considering that oxygen atom possesses atomic radii similar to C or N atoms. For example, Yu et al.[11] demonstrated oxygen doped of hierarchically porous g-C_3N_4 tubes by thermal oxidation exfoliation at 600 °C. They achieved a narrow band gap of 2.61 eV in the doping g-C_3N_4 which was endowed with enhanced photocatalytic CO_2 reduction compared with bulk g-C_3N_4 (2.75 eV). A porous oxygen doped g-C_3N_4 through thermal poly-condensation at 500 °C prepared by Yang et al.[14] showed a band gap decreases from 2.7 to 2.5 eV, exhibiting an enhanced (~ 5 times) photocatalytic hydrogen production performance compared with the pristine g-C_3N_4 under visible light. Undeniably, doping g-C_3N_4 has attracted significant research and industry interest. Development of facile, large-scale production strategies for doping g-C_3N_4 represents an important step towards the realization of its application potential.

Recently, several groups have used solvothermal approach to synthesize g-C_3N_4 at relatively low temperature (< 220 °C).[15, 16] Such a singular solvothermal method *via* assembling large polymeric superstructures at low

[a] *State Key Laboratory of Advanced Technology for Materials Synthesis and Processing, Wuhan University of Technology, 122 Luoshi Road, 430070, Wuhan, Hubei, China; Fax:+86 27 87879468; Tel: +86 27 87855322. Email: yu.li@whut.edu.cn*
[b] *Cambridge Graphene Centre, University of Cambridge, 9 JJ Thomson Avenue, Cambridge CB3 0FA, United Kingdom.*
[c] *Laboratory of Inorganic Materials Chemistry, University of Namur, 61 rue de Bruxelles, B-5000 Namur, Belgium.*
[d] *Clare Hall, University of Cambridge, Herschel Road, Cambridge CB3 9AL, United Kingdom.*

Electronic Supplementary Information (ESI) available: The raw material molar ratios of DCNA and CC, XPS results, the rate constants of RhB degradation on the samples and the structure of g-C_3N_4 with labelled O and N sites for DFT calculations. See DOI: 10.1039/x0xx00000x

temperature is very attractive. This is because it enables a rational bottom-up design of g-C_3N_4 by molecular engineering, solution phase assembly, crystallization, and covalent cross-linking chemistry in a "one-pot" method. In addition, it provides an abundant choice of appropriate co-monomers and content with diverse chemical composition and structure to achieve modification of the electronic band structure and optoelectronic properties of the synthesized material. However, achieving oxygen doping or other non-metal doping in g-C_3N_4 is still challenging at low synthesis temperature.

Here, we present a detailed investigation on oxygen self-doped g-C_3N_4 to tune its electronic band structure *via* directly exposing the solvothermally synthesized g-C_3N_4 in the ambient environment. To the best of our knowledge, this is the first example of oxygen self-doped g-C_3N_4 that does not require specific doping protocols during the synthesis process. In particular, we demonstrate that the oxygen content and thus the doping process can be controlled by copolymerization of the precursors. Our oxygen self-doped g-C_3N_4 exhibits highly enhanced activities for RhB degradation and H_2 production under visible light compared to the typical thermally made g-C_3N_4. More importantly, the excellent stability of oxygen self-doped g-C_3N_4 enables long lasting degradation and H_2 production. This new type of highly stable, self-doping, metal-free semiconductor sheds new light on the development of low-cost photocatalysts for long-term solar fuel production with high transition efficiency.

Experimental section

Materials

Dicyandiamide (DCNA), melamine and acetonitrile were purchased from Shanghai Aladdin Biochemical Technology Co., Ltd. 1,3,5-trichlorotriazine (CC) was purchased from Shanghai Jingchun Biochemical Technology Co., Ltd. Anhydrous ethanol was purchased from Sinopharm Chemical Reagent Co., Ltd. All the chemical reagents were used as received.

Synthesis of CN-pure and oxygen doping CNO-x

The pure g-C_3N_4 was prepared by directly heating melamine (10.0 g) at a rate 5 °C min^{-1} to reach a temperature of 550 °C, and then maintain at this temperature for 2 h in environment atmosphere. Finally the sample was naturally cooled down to room temperature. The final product was denoted as CN-pure.

Typically, 5 mmol 1,3,5-trichlorotriazine (CC) was dissolved in 50 mL acetonitrile accompanying with different amounts (2.5, 5, 10, and 20 mmol) of dicyandiamide (DCNA) addition *via* continuous stirring at room temperature for 2 h. The mixture was transferred into a 100 mL teflon-lined autoclave, which was sealed and maintained at 200 °C for 24 h. After cooling to room temperature, the product was washed with distilled water and ethanol for several times. The final product was obtained after drying at 60 °C for 12 h, and denoted as CNO-x, where x represents to the raw material molar ratios of DCNA and CC (x = 0.5, 1, 2 and 4), as shown in **Table S1**.

Decoration of Pt nanoparticles on CN-pure and CNO-x

Typically, 0.2 g of the as-prepared sample (CN-pure or CNO-x) was added into 20 mL aqueous solution containing 2.5 mL H_2PtCl_6 (1 mg/mL) with continuous stirring for 1 h. Subsequently, 15 mL aqueous solution of $NaBH_4$ (0.05 M) and trisodium citrate dihydrate (0.01 M) was added into the above mixture for 2 h. During this process, Pt^{4+} in H_2PtCl_6 was reduced by $NaBH_4$ to form Pt^0 on the surface. Then, the sample was collected by centrifugation and thoroughly washed with deionized water before drying in an oven at 60 °C for 12 h.

Characterizations

Crystallographic phases of the prepared products were investigated by X-ray diffraction (XRD) using a Bruker D8 advance with Cu Kα radiation (40 kV, 40 mA). The morphologies of the samples were characterized by a field-emission scanning electron microscopy (FESEM, Hitachi S-4800), transmission electron microscopy (TEM, JEOL JEM-2100F) at an acceleration voltage of 200 kV. X-ray photoelectron spectroscopy (XPS) was carried out on a customized X-ray photoelectron spectrometer (VG Multilab 2000-X equipped with a monochromatic Al Kα source). The UV–Vis absorption spectra were collected by SHIMADZU UV–Vis spectrophotometer in the spectral range 200-800 nm. The content of Pt was measured by an Inductively Coupled Plasma Emission Spectrometer (ICP-AES, PerkinElmer Optima 4300DV). The Photo-electrochemical analysis was carried out on Autolab PGSTAT 302N equipment in the frequency range of 1Hz to 1000 Hz.

Computational method

All calculations were performed using the generalized gradient approximation (GGA) and Perdew-Burkee-Ernzerhof (PBE) exchange-correlation functional, as implemented in the $Dmol^3$ package of Material Studio, which were the first principles pseudopotential methods based on DFT. The Band Structure and Density of States (DOS) were calculated using $Dmol^3$ program. The core electrons were treated by the all electron relativistic method and the basic set of double numerical plus polarization (DNP) was used. The convergence tolerances for geometry optimization calculations were set to the maximum displacement of 0.002 Å, the maximum force of 0.05 eV/Å, and the maximum energy change of 2.0×10^{-5} eV/$atom^{-1}$. The SCF convergence tolerance was set to 2.0×10^{-6} eV/atom.

Photoelectrochemical characterization

Photoelectrochemical measurements for Mott–Schottky plots were performed on three-electrode system using an electrochemical workstation (Autolab PGSTAT 302N). The cleaned FTO glass deposited with samples, Pt and Ag/AgCl electrode were used as working electrode, counter electrode, and reference electrode, respectively. The light source was a LED (3 W, 420 nm) and 0.5 M Na_2SO_4 aqueous solution acted as the electrolyte. The electrochemical impedance spectra (EIS) were recorded over a frequency range of 1–1000 Hz with an amplitude of 5 mV at the same bias voltages. Mott–

Schottky plots were recorded by using the Impedance-Potential mode.

Photocatalytic activity

Photocatalytic activity was evaluated by the Rhodamine B (RhB) in an aqueous solution under visible light irradiation (λ > 420 nm). In the experiment, 0.05 g of photocatalyst (CN-pure or CNO-x without Pt) was dispersed in RhB solution (100 mL, 10^{-5} mol/L). Prior to irradiation, the suspension was magnetically stirred in the dark for 30 min to reach adsorption-desorption equilibrium. At certain time intervals, 2 mL aliquots were sampled and centrifuged to remove the particles. The filtrates were analyzed by recording variations in the absorption peak position (554 nm for RhB) using UV2550 (SHIMADZU) UV–Vis spectrometer.

The photocatalytic hydrogen evolution measurements were carried out in a closed circulation system using a PLS-SXE-300C lamp (Beijing Perfectlight Science & Technology Co., LTD) with a visible light intensity of 158 mW/cm^2. 0.02 g sample (CN-pure or CNO-x with 0.3 wt% Pt) was immersed in an aqueous solution (100 mL) containing triethanolamine (10 vol. %) as the sacrificial electron donor. The mixture was sealed in a quartz vessel and stirred during photoreaction. After degassing, the vessel was irradiated under visible light (420–780 nm). The gas products were analyzed periodically by an Agilent 7890A gas chromatograph (GC) with a thermal conductivity detector (TCD).

Results and discussion

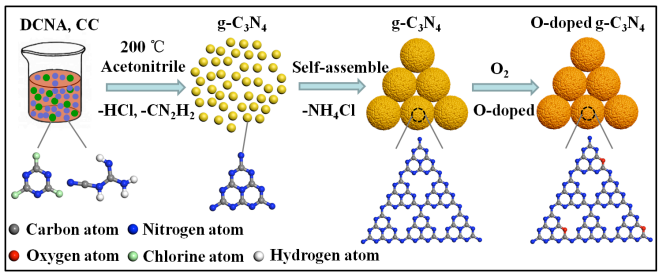

Figure 1. Illustration of the formation process of oxygen self-doped g-C_3N_4 nanospheres (CNO-x).

Figure 1 illustrates the process of oxygen self-doped g-C_3N_4 *via* copolymerization through solvothermal method. In this strategy, dicyandiamide (DCNA) is used as the main precursor, and 1,3,5-trichlorotriazine (CC) as the crystal structure regulator to adjust the ordering of the crystal structure and then to regulate the oxygen doping. **Figure S1** demonstrates the detailed polymerization steps of DCNA and CC. 1,3,5-trichlorotriazine (CC) is selected as a precursor because it can react with dicyandiamide (DCNA) to give intermediate **i**. The intermediate **p** is formed by condensation of DCDA. Experimentally, a series CC-functionalized g-C_3N_4 polymers are synthesized by changing the amount of CC added to DCDA for copolymerization. **Table S1** shows the molar mass of DCNA and CC. The samples are denoted as CNO-0.5, CNO-1, CNO-2 and CNO-4 according to the molar ratio of DCNA and CC. To illustrate the advantage of our synthesis strategy for oxygen self-doped g-C_3N_4 photocatalysts, pure g-C_3N_4 *via* solid-state synthesis at high temperature was also prepared (denoted as CN-pure).

Figure 2a presents the SEM images of CN-pure from solid-state route, which obviously shows the layered structure. While the morphology of CNO-1, CNO-2 and CNO-4 from the solvothermal method is an irregular spherical structure composed of nanoparticles (**Figure 2c,d,e**). However, CN-0.5 has a quite different morphology of spheres with a smooth surface (**Figure 2b**). This indicates that CC can strongly affect the polymerization process of CNO-x. **Figure 2f** displays a typical TEM image of the synthesized CNO-4, showing the interconnected nanoparticles of ~10 nm diameter. Such small nanoparticles are beneficial for oxygen self-doped g-C_3N_4 to tune its electronic band structure.

Figure 3a shows the XRD patterns of the CN-pure and CNO-x samples. The patterns indicate that the CN-pure sample has two distinct peaks at 13.1° and 27.4°, indexed as (100) and (002) diffraction planes.[17] However, the peak at 27.4° of CNO-0.5, CNO-1, CNO-2 and CNO-4 is shifted significantly toward a lower 2θ value while the peak at 13.1° disappears. We hypothesize that this crystal lattice distortion arises from the defects (such as oxygen doping) in the g-C_3N_4 network.[14] In addition, the broadened peak at 27.4° of the CNO-x samples indicates a much smaller crystal compared to that of the CN-pure sample.

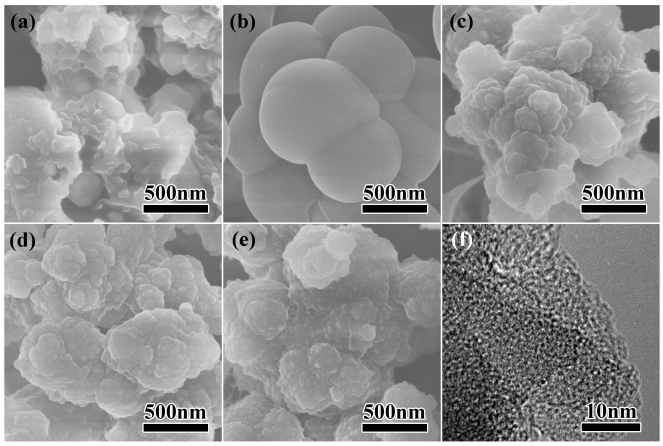

Figure 2. SEM images of (a) CN-pure, (b) CNO-0.5, (c) CNO-1, (d) CNO-2, and (e) CNO-4. (f) TEM image of CNO-4.

Fourier transform infrared (FTIR) spectroscopy of these samples was conducted to further investigate the oxygen self-doped g-C_3N_4 (**Figure 3b**). The broad absorption band at 3100–3300 cm^{-1} can be assigned to the stretching modes of secondary and primary amines and their intermolecular hydrogen bonding interactions. The band at 1200–1600 cm^{-1} corresponds to the aromatic carbon nitride heterocycles, the absorption band at 884 cm^{-1} is ascribed to deformation of N–H and the band at 810 cm^{-1} belongs to tri-3s-triazine ring modes.[15, 18] Compared to CN-pure, the FTIR spectrum of CNO-x shows two new bands at 975 cm^{-1} and 2180 cm^{-1}. The former can be assigned to the stretching of C–O–C and the latter is vested in the appearance of C≡N or N=C=N, due to the

incomplete polymerization of precursors.[19, 20] Notably, the peaks at 1240, 1327, 1410 and 1640 cm^{-1} in CN-pure depict a slight shift of 1262, 1316, 1438 and 1615 cm^{-1} respectively in the CNO-x samples. It can be inferred that the bond strength of C–N is changed after oxygen doping in CNO-x.

UV–Vis reflectance spectroscopy was carried out to investigate the band gap of these samples. In **Figure 3c**, compared to the CN-pure, the absorption wavelength range of the CNO-x samples is noticeably red-shift, indicating that oxygen doped CNO-x can be beneficial for extending the absorption range of light. As g-C_3N_4 is a indirect band gap semiconductor, plots of the $(\alpha hv)^2$ versus the energy of absorbed light can help estimating the band gaps of samples as shown in **Figure 3d**, where α is the absorption coefficient.[21] The calculated band gaps are approximately 2.73, 2.54, 2.32, 2.21 and 2.09 eV for CN-pure, CNO-0.5, CNO-1, CNO-2 and CNO-4, respectively. The CNO-4 can narrow the band gap of g-C_3N_4 by 0.64 eV. This indicates that the band structure of g-C_3N_4 is changed by oxygen doping, which is in agreement with the results of XRD and FTIR. We propose that the band gap of CNO-x is tunable due to change in the doping density while the co-monomer CC content is controlled.[22]

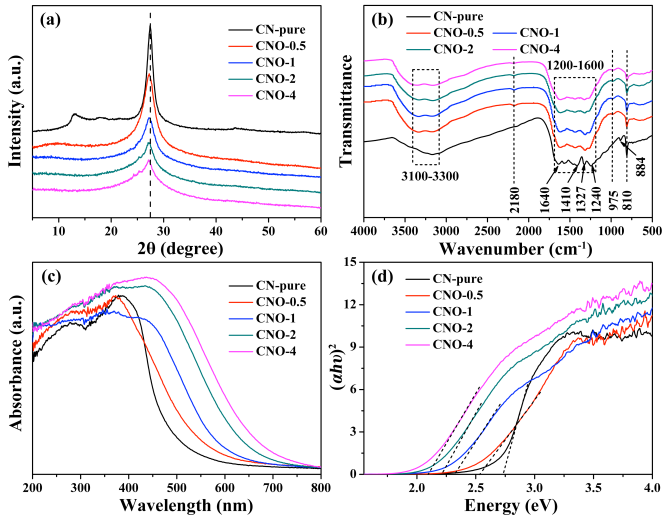

Figure 3. (a) XRD, (b) FTIR spectra, (c) UV-Vis and (d) Plots of $(\alpha hv)^2$ versus the energy of the CN-pure and CNO-x.

X-ray photoelectron spectroscopy (XPS) was conducted to verify the oxygen self-doped CNO-x samples. In the XPS survey spectra of CN-pure and CNO-4 (**Figure 4a**), only O 1s, N 1s, and C 1s peaks of CN-pure could be observed. Interestingly, the slight Cl $2p^3$ peak of CNO-4 is found compared with CN-pure, indicating small amounts of Cl atoms in CNO-4. This result corresponds to the reaction mechanism diagram (**Figure S1**). The intensity of O 1s peak of CNO-4 is much stronger than that of CN-pure. However, the intensity of N 1s peak of CNO-4 is much weaker than that of CN-pure, indicating more O atoms and less N atoms in CNO-4. We assume that part of the N atoms are replaced by O atoms. As displayed in the O 1s spectra (**Figure 4b**), the single peak at 532.4 eV of O 1s in CN-pure corresponds to the adsorbed H_2O. There are three kinds of O species in the CNO-4, with binding energies at 531.6, 533.0 and 534.0 eV, respectively. These correspond to N–C–O, C–O–C and adsorbed O_2, respectively.[17, 23] In the reaction system of CNO-x, the oxygen may be self-doping into g-C_3N_4 lattice after the synthesized products are exposed in the ambient since no chemicals with oxygen have been added. This proposal is reasonable considering that partial of nitride atoms of the CC functional group in the g-C_3N_4 polymers network are deficient or not stable in air and can be easily oxidized.

As shown in C 1s spectra (**Figure 4c**), the spectrums of CN-pure and CNO-4 are divided into three and four kinds of C species, respectively. The peak at 284.6 eV originates from adventitious carbon (sp^3 C–C), while the peaks at 288.0 eV or 288.1 eV (N=C–N) and 288.6 eV (C=N) are ascribed to carbon at the two different spatial locations in the basic aromatic CN heterocycles.[13, 16] Two new peaks at 286.8 eV and 289.1 eV correspond to C–O–C and C–O bonds in the C 1s spectrum of CNO-4. This is consistent with the assumption that O atoms are doped into the matrix of CN heterocycles by bonding with C atoms.[19, 24, 25] In order to study the location of O atoms in the CN matrix, **Figure 4d** presents the N 1s spectra of CN-pure and CNO-4. The peaks at 398.6 eV (or 398.7 eV), 399.8 eV (or 400.0 eV) and 404.4 eV can be ascribed to sp^2-hybridized nitrogen C–N=C, sp^3-hybridized nitrogen N–$(C)_3$ and C=N in the aromatic CN heterocycles, respectively. Both samples show a peaks at 401.0 eV, deriving from the N atom of the amino functional groups with a hydrogen atom (C–N–H).[26-28] The results of N 1s spectra of CNO-4 indicate that the intensity ratio of N (sp^2)/N (sp^3) decreases from 4.26 to 1.93 (**Table S2**) and the C/N atomic ratio increases from 0.69 to 1.08 after oxygen doping (**Table S3**).[17] All these data demonstrate that some sp^2-hybridized nitrogen atoms in the CNO-4 lattice are substituted by oxygen atoms, leading to the decreased N (sp^2)/N (sp^3) ratio and increased C/N atomic ratio.[12] Moreover, a similar increasing tendency of the C/N atomic ratio is also detected by elemental analysis of CN-pure and CNO-x. As shown in **Figure S2** and **S3**, the XPS survey spectra and high resolution O 1s, C 1s, N 1s XPS spectra of CNO-1 and CNO-2 (**Table S4-S6**) have similar results with the CNO-4.

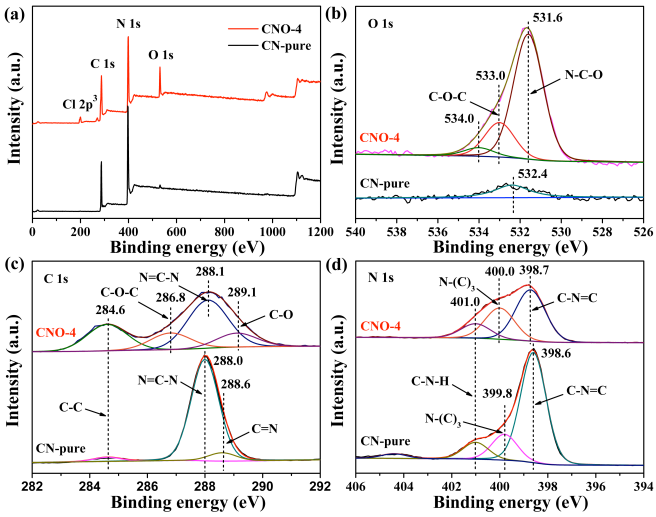

Figure 4. (a) XPS survey spectra and High resolution (b) O 1s, (c) C 1s, (d) N 1s XPS spectra of CN-pure and CNO-4.

The effect of oxygen doping to tune the electronic band structure of g-C_3N_4 was calculated *via* the first-principles pseudopotential methods based on density functional theory (DFT). For the lamellar structure of tri-3s-triazine based g-C_3N_4, there are three N sites and two C sites, which are labelled as N1, N2, N3, C1 and C2, respectively (**Figure 4S**). **Figure 5a** and **5c** show the CN-pure and CNO-x (O doped in N2 site) models with 42 atoms in one unit cell.[29, 30] The calculated band structures and DOS of CN-pure and CNO-x are presented in **Figure 5b** and **5d**, respectively, in which the value of energy equal to zero is set as the Fermi level. It shows that the band gap of CN-pure is narrowed after the substitution of edge N2 with O.[31] To reveal the contributions of each related orbital to the band, the total density of state (TDOS) and partial density of state (PDOS) are as well as displayed in **Figure 5b** and **5d**. It can be seen that the valance band edge of CN-pure is mainly contributed by the N2 and small amounts of C1 and N1 atoms states, and the conduction band edge is dominated by the states of C (both C1 and C2) atoms and inner N1 atoms. The DOS of CNO-x show that the valance band is mainly dominated by the N1 and N2 atoms, and the conduction band is composed of the C2 and N1 atoms and small amounts of N2 and O atoms. This reveals that the CNO-x samples are more favorable for enhancing the carrier mobility, effectively separating the photogenerated electron–hole pairs, increasing light absorption and reducing work function.

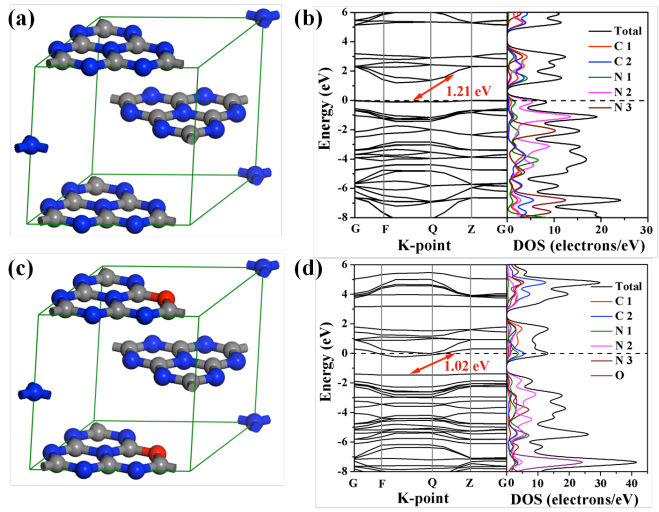

Figure 5. DFT calculations of the models of (a) CN-pure and (c) CNO-x. Calculated band structure and the corresponding DOS of (b) CN-pure and (d) CNO-x.

In order to make sure the positions of band edges of CNO-x, their electronic band structures were examined *via* Mott–Schottky plots compared to CN-pure. As shown in **Figure 6a-b** and **Figure S5**, the Mott–Schottky plots of CN-pure and CNO-x exhibit positive slopes at various frequencies (from 1 to 1000 Hz). This is a typical characteristic of n-type semiconductors.[32] The Mott–Schottky plots of CNO-x show a smaller slope than that of CN-pure, suggesting a higher electron donor density for CNO-x. A high donor density, possibly caused by oxygen doping, is very helpful for improving photocatalytic performance because of the increased electrical conductivity and the mobility of charge carriers.[33] The flat band potentials derived from the x-intercept in the Mott–Schottky plots of CN-pure and CNO-x are −1.02, −1.42, −1.37, −1.30 and −1.25 V versus the saturated Ag/AgCl reference electrode (pH = 7), respectively.[34] The 0.23 to 0.40 V down shift of the conduction band should be caused by oxygen doping of CNO-x. The lower flat band potential also indicates more positive conduction band (CB) potential of CNO-x compared to CN-pure. The narrower band gap of CNO-x is in agreement with the red shift of the intrinsic absorption edge in UV–Vis spectra. The CB potential is very close to the flat band potential in n-type semiconductors.[11, 32, 35] Based on the band gap derived from the UV–Vis spectra, the corresponding band gap structures of CN-pure and CNO-x are shown in **Figure 6c**. The band structure thermodynamically is suitable for photocatalytic organic pollutants degradation and hydrogen evolution under visible light. These are also reflected much smaller diameter of the semicircular Nyquist curve of electrochemical impedance spectroscopy under visible light radiation (**Figure 6d**). Note that the arc radius of the Nyquist plot CNO-x is smaller than that of CN-pure, implying a smaller charge transfer resistance of CNO-x.[36, 37] This leads to better conductivity and faster charge transfer of CNO-x, in good agreement with the results of the Mott–Schottky results.

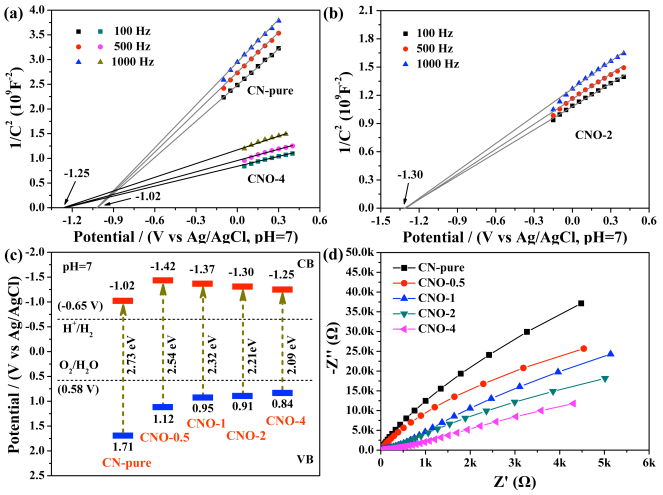

Figure 6. (a) Mott–Schottky plots collected at various frequencies of CN-pure and CNO-4. (b) Mott–Schottky plots collected at various frequencies of CNO-2. (c) bandgap structures of CN-pure and CNO-x versus the saturated Ag/AgCl reference electrode (pH = 7) (CB: conduction band; VB: valence band). (d) EIS Nyquist plots of CN-pure and CNO-x under visible light (λ > 420 nm).

The photocatalytic activities of the samples were evaluated for Rhodamine B (RhB) photodegradation under visible light (λ > 420 nm). Compared to CN-pure, the CNO-x samples demonstrate enhanced photocatalytic activity under visible light irradiation for 60 min (**Figure 7a**). In particular, CNO-4 can completely degrade RhB (100 mL, 10^{-5} mol/L) in 15 min under visible light, much faster than other oxygen self-doped CNO-x (x = 0.5, 1, 2) samples. First-order kinetics is attempted to fit the data *via* a linear plot of ln(C_0/C) against time to determine the photocatalytic reaction rate. **Figure 7b** reveals that the photocatalytic reaction rates follow the principle of kinetics pseudo first-order reaction.[38] The photodegradation rate constants of RhB for CN-pure and CNO-x are 0.007, 0.051, 0.072, 0.142 and 0.249 min^{-1} (**Figure S6**), respectively. Namely, the photodegradation rates of CNO-x are ~7, ~10, ~20 and~36 times, respectively, compared to that of CN-pure without

oxygen doping. This shows that the increase in oxygen doping content improves the photocatalytic performance of CNO-x. This indicates that the oxygen doping facilitates the transport of electrons and broadens the light absorption range in CNO-x.

Since the catalyst's lifetime is an important parameter in the photocatalytic process, the stability of the CNO-4 photocatalyst is investigated. The result presented in **Figure 7c** shows no obvious loss of photocatalytic performance after 5 cycles. The mechanism for photodegradation of RhB of the CNO-x samples is further investigated. We select the CNO-1 sample for this since the photodegradation rate of CNO-4 is too fast. The main oxidative species during the photocatalytic process can be detected through trapping electron (e^-) and holes (h^+) by using $AgNO_3$ (0.01M, electron scavenger) and triethanolamine (TEOA, 0.01M, hole scavenger), respectively.[21, 39] As shown in **Figure 7d**, one can see that the addition of $AgNO_3$ can cause an enhanced photodegradation of RhB while the photocatalytic activity can be greatly suppressed by the addition of TEOA in CNO-1. This indicates that the oxygen self-doped CNO-x rely on photogenerated holes for RhB degradation.

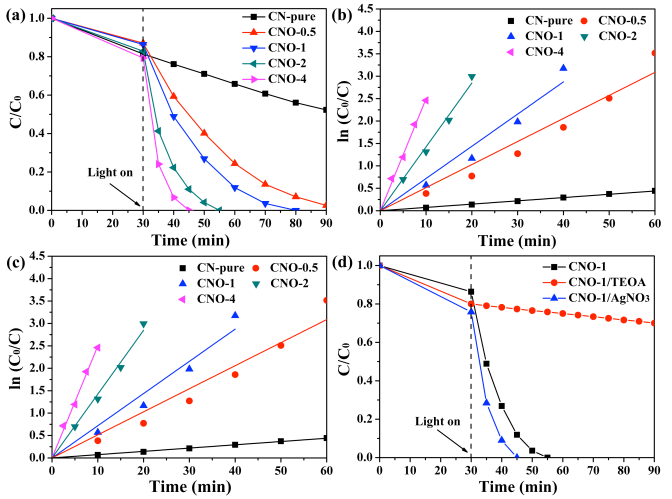

Figure 7. The photocatalytic degradation of RhB for the CN-pure and CNO-x photocatalysts under visible light (λ > 420 nm). (a) The process of photocatalytic degradation of RhB. (b) The plots of $\ln(C_0/C)$ vs reaction time for the photocatalytic degradation of RhB. (c) The cycling performance of CNO-4. (d) The plots of photogenerated carriers trapping in the system of photodegradation of RhB by CNO-1.

The photocatalytic activities of CNO-x were next evaluated for photocatalytic H_2 production （**Figure 8a**） under visible light using Pt as the co-catalyst and triethanolamine as the hole scavenger. The loading of Pt (**Table S7**) is ~0.3 wt%, as measured by an Inductively Coupled Plasma Emission Spectrometer (ICP). All the CNO-x samples demonstrate highly enhanced photocatalytic H_2 production compared to that of the CN-pure sample. For example, CN-pure gives a low activity with H_2 production rate of 846 μmol h^{-1} g^{-1}, while CNO-0.5, CNO-1, CNO-2 and CNO-4 show a higher H_2 generation rate of 1837, 2257, 3174 and 2772 μmol h^{-1} g^{-1}, respectively (**Figure 8b**). We propose that the oxygen doping increases carrier mobility. This, coupled with broadening of light absorption spectrum in the CNO-x greatly enhances H_2 production. We note that CNO-2 exhibits the highest hydrogen production, which is nearly 4 times that of CN-pure. A reduction in the sample of CNO-4 is attributed to its narrowest band gap among the CNO-x samples, which may result in faster recombination of the photogenerated carriers. To evaluate the stability of CNO-2, the reaction achieves the rate of 2965 μmol h^{-1} g^{-1} with excellent performance stability in 5 photocatalytic cycles up to 25 h under visible light irradiation (**Figure 8c**). These results demonstrate that the oxygen doping in g-C_3N_4 can strongly enhance its photocatalytic performance.

A reason for the high activity of the CNO-x samples can be accredited to lower CB potentials and narrowed band gaps compared to pristine CN-pure. But this case is not enough to engender the great enhancement in photocatalytic activity. In **Figure 8d**, the photocurrent responses of the synthesized samples were measured to qualitatively analyse the separation efficiency of electron–hole pairs. It is clearly seen that the photocurrents of the CNO-x samples have better efficiencies of photo-generated charge separation and transport comparing with the CN-pure sample. This is very beneficial for photocatalytic activity.[40-42] Meanwhile, the photocurrent of CNO-2 is the highest among all the oxygen self-doped CNO-x samples. This result is consistent with the hydrogen production performance.

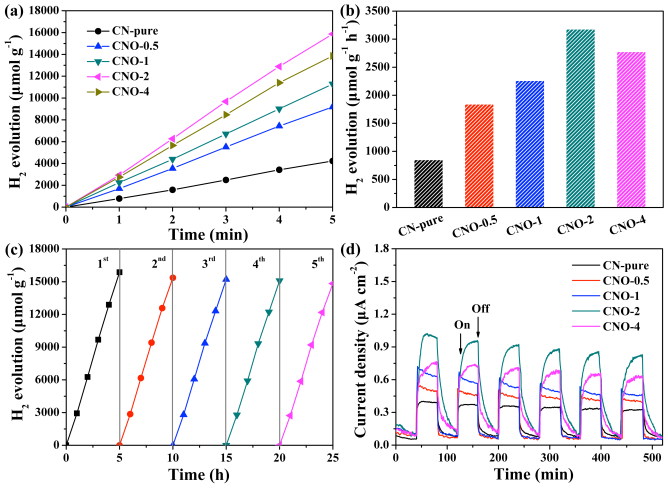

Figure 8 The photocatalytic H_2 production for the CN-pure and CNO-x under visible light (λ > 420 nm). (a) The hydrogen production and (b) hydrogen production rates of the CN-pure and CNO-x with 0.3 wt% Pt. (c) The cycling reaction of CNO-2 with 0.3 wt% Pt for 5 cycles. (d) Transient photocurrent responses of CN-pure and CNO-x under visible light (λ > 420 nm).

Based on the results and discussions above, we propose that oxygen doping can broaden the visible light response region of g-C_3N_4 and modification of its band structure and electronic property. In CNO-x redox reaction of RhB, the photogenerated holes are the main oxidative species. In the photocatalytic reaction for hydrogen production, the photogenerated electrons transfer from conduction band (CB) of CNO-x to Pt nanoparticles, which act as the electron acceptor. Hydrogen is then produced on these active sites. In addition, TEOA serves as an electron donor, reacting with the photogenerated holes in the valence band (VB) of CNO-x. The mechanisms for the degradation of RhB and splitting of water for hydrogen production under visible light are schematically illustrated in **Figure 9**.

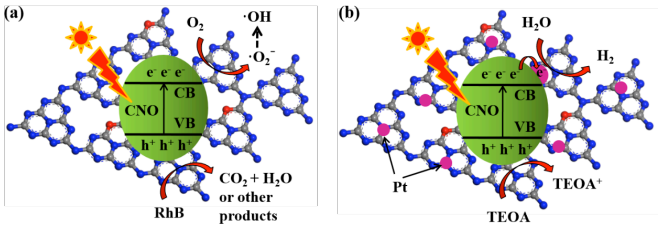

Figure 9. (a) Proposed mechanism of photocatalytic degradation of RhB. (b) and hydrogen evolution by the CNO photocatalyst under visible light irradiation.

Conclusions

In summary, a series of oxygen self-doped CNO-x photocatalyst is successfully fabricated *via* a solvothermal method. The introduction of oxygen is proved to efficiently modulate the electronic band gap structure through simulated calculation and experimental results. Comparing to the traditional g-C_3N_4 with band gap 2.73 eV, the oxygen doped CNO-x exhibit narrowed band gaps from 2.54 to 2.09 eV. This ensures that the as-prepared CNO-x samples exhibit highly enhanced photocatalytic performance, as demonstrated through the degradation of RhB and splitting of water for H_2 production under visible light. The significant enhancement of photocatalytic activity could be ascribed to the synergistic effects of narrowed band gap and improved charge transfer efficiency. We believe that this new type of highly stable doping of metal-free semiconductor develops an effective pathway for the design of photocatalysts with high photoactivity.

Acknowledgements

Y. Li acknowledges Hubei Provincial Department of Education for the “Chutian Scholar” program. B. L. Su acknowledges the Chinese Central Government for an “Expert of the State” position in the Program of the “Thousand Talents” and a Life Membership at the Clare Hall, Cambridge and the financial support of the Department of Chemistry, University of Cambridge. T. Hasan acknowledges support from the Royal Academyof Engineering (Graphlex). This work is supported by the National Key R&D Program of China (2016YFA0202602), Program for Changjiang Scholars and Innovative Research Team in University (IRT-15R52), National Natural Science Foundation of China (U1663225, 21671155) and the Fundamental Research Funds for the Central Universities (WUT: 2016III029).

Notes and references

1 Z. W. Li, G. D. Jiang, Z. H. Zhang, Y. Wu and Y. H. Han, *Journal of Molecular Catalysis A: Chemical*, 2016, **425**, 340-348.
2 S. W. Cao, J. X. Low, J. G.Yu and M. Jaroniec, *Adv. Mater.*, 2015, **27**, 2150-2176.
3 X. C. Wang, S. Blechert and M. Antonietti, *ACS Catalysis*, 2012, **2**, 1596-1606.
4 C. M. Li, Y. H. Du, D. P. Wang, S. M. Yin, W. G. Tu, Z. Chen, M. Kraft, G. Chen and R. Xu, *Adv. Funct. Mater.*, 2017, **27**, 1604328.
5 M. V. González, W. C. Liao, R. Cazelles, S. Wang, X. Yu, V. Gutkin and I. Willner, *ACS Nano*, 2017, **11**, 3247-3253.
6 X. G. Li, W. T. Bi, L. Zhang, S. Tao, W. S. Chu, Q. Zhang, Y. Luo, C. Z. Wu and Y. Xie, *Adv. Mater.*, 2016, **28**, 2427-2431.
7 Z. L. Ni, F. Dong, H. W. Huang and Y. X. Zhang, *Catal. Sci. Technol.*, 2016, **6**, 6448-6458.
8 J. L. Miao, G. Q. Xu, J. Q. Liu, J. Lv and Y. C. Wu, *Journal of Solid State Chemistry*, 2017, **246**, 186-193.
9 G. G. Liu, T. Wang, H. B. Zhang, X. G. Meng, D. Hao, K.Chang, P. Li, T. Kako and J. H. Ye, *Angew. Chem. Int. Ed.*, 2015, **54**, 1-6.
10 S. Y. Zhang, L. N. Gao, D. L. Fan, X. M. Lv, Y. Li and Z. X. Yan, *Chemical Physics Letters*, 2017, **672**, 26-30.
11 J. W. Fu, B. C. Zhu, C. J. Jiang, B. Cheng, W. You and J. G. Yu, *Small*, 2017, **13**, 1603938
12 K. Wang, Q. Li, B. S. Liu, B. Cheng, W. K. Ho and J. G. Yu, *Applied Catalysis B: Environmental*, 2015, **176-177**, 44-52.
13 G. G. Zhang, M. W. Zhang, X. X. Ye, X. Q. Qiu, S. Lin and X. C. Wang, *Adv. Mater.*, 2014, **26**, 805-809.
14 L. J. Fang, X. L. Wang, J. J. Zhao, Y. H. Li, Y. L. Wang, X. L. Du, Z. F. He, H. D. Zeng and H. G.Yang, *Chem. Commun.*, 2016, **52**, 14408-14411.
15 Y. X. Wang, H. Wang, F. Y. Chen, F. Cao, X. H. Zhao, S. G. Meng and Y. J. Cui, *Applied Catalysis B: Environmental*, 2017, **206**, 417-425.
16 Q. Gu, Z. W. Gao and C. Xue, *Small*, 2016, **12**, 3543-3549.
17 J. H. Li, B. Shen, Z. .H. Hong, B. Z. Lin, B. F. Gao and Y. L. Chen, *Chem. Commun.* , 2012, **48**, 12017-12019.
18 Y. J. Wang, R. Shi, J. Lin and Y. F. Zhu, *Energy Environ. Sci.*, 2011, **4**, 2922.
19 H. Wang, S. L. Jiang, S. C. Chen, D. D. Li, X. D. Zhang, W. Shao, X. S. Sun, J. F. Xie, Z. Zhao, Q. Zhang, Y. P. Tian and Y. Xie, *Adv. Mater.*, 2016, **28**, 6940-6945.
20 W. J. Ong, L. L. Tan, S. P. Chai and S. T. Yong, *Chem. Commun.*, 2015, **51**, 858-861.
21 G. H. Dong and L. Z. Zhang, *J. Mater. Chem.*, 2012, **22**, 1160-1166.
22 Z. A. Lan, G. G. Zhang and X. C. Wang, *Applied Catalysis B: Environmental*, 2016, **192**, 116-125.
23 Z. K. Zhao, Y. T Dai, J. H. Lin and G. R. Wang, *Chem. Mater.*, 2014, **26**, 3151-3161.
24 C. H. Li, X. L. Kang, Q. H. Zhu and W. G. Zheng, *Applied Surface Science,* 2017, **398**, 89-96.
25 Q. H. Liang, Z. Li, X. L. Yu, Z. H. Huang, F. Y. Kang and Q. H. Yang, *Adv. Mater.*, 2015, **27**, 4634-4639.
26 G. G. Zhang, C. J. Huang and X. C. Wang, *Small*, 2015, **11**, 1215-1221.
27 G. X. Zhao, G. G. Liu, H. Pang, H. M. Liu, H. B. Zhang, K. Chang, X. G. Meng, Xi. J. Wang and J. H. Ye, *Small*, 2016, **12**, 6160-6166.
28 Y. B. Li, H. M. Zhang, P. R. Liu, D. Wang, Y. Li and H. J. Zhao, *Small*, 2013, **9**, 3336-3344.
29 B. C. Zhu, J. F. Zhang, C. J. Jiang, B. Cheng and J. G. Yu, *Applied Catalysis B: Environmental*, 2017, **207**, 27-34.

30 S. Lu, Z. W. Chen, C. Li, H. H. Li, Y. F. Zhao, Y. Y. Gong, L. Y. Niu, X. J. Liu, T. Wang and C. Q. Sun, *J. Mater. Chem. A*, 2016, **4**, 14827-14838.
31 J. Cui, S. H. Liang, X. H. Wang and J. M. Zhang, *Materials Chemistry and Physics*, 2015, **161**, 194-200.
32 Q. H. Liang, Z. Li, Z. H. Huang, F. Y. Kang and Q. H. Yang, *Adv. Funct. Mater.*, 2015, **25**, 6885-6892.
33 Z. F. Huang, J. J. Song, L. Pan, Z. M. Wang, X. Q. Zhang, J. J. Zou, W. B. Mi, X. W. Zhang and L. Wang, *Nano Energy*, 2015, **12**, 646-656.
34 G. G. Liu, G. X. Zhao, W. Zhou, Y. Y. Liu, H. Pang, H. B. Zhang, D. Hao, X. G. Meng, P. Li, T. Kako and J. H. Ye, *Adv. Funct. Mater.*, 2016, **26**, 6822-6829.
35 M. Ou, S. P. Wan, Q. Zhong, S. L. Zhang, Y. Song, L. N. Guo, W. Cai and Y. L. Xu, *Applied Catalysis B: Environmental*, 2018, **221**, 97-107.
36 B. Lin, H. Li, H. An, W. B. Hao, J. J. Wei, Y. Z. Dai, C. S. Ma and G. D. Yang, *Applied Catalysis B: Environmental*, 2018, **220**, 542-552.
37 O. Elbanna, M. Fujitsuka and T. Majima, *ACS Appl. Mater. Interfaces*, 2017, **9**, 34844-34854.
38 W. Liu, M. L. Wang, C. X. Xu and S. F. Chen, *Chemical Engineering Journal*, 2012, **209**, 386-393.
39 S. Chu, Y. Wang, Y. Guo, J. Y. Feng, C. C. Wang, W. J. Luo, X. X. Fan and Z. G. Zou, *ACS Catal.*, 2013, **3**, 912-919.
40 C. W. Yang, J. Q. Qin, Z. Xue, M. Z. Ma, X. Y. Zhang and R. P. Liu, *Nano Energy*, 2017, **41**, 1-9.
41 Y. N. Ma, J. Li, E. Z. Liu, J. Wan, X. Y. Hu and J. Fan, *Applied Catalysis B: Environmental*, 2017, **219**, 467-478.
42 Q. Liu, T. X. Chen, Y. R. Guo, Z. G. Zhang and X. M. Fang, *Applied Catalysis B: Environmental*, 2016, **193**, 248-258.

